Multifrequency Radiometric Determination of Temperature Profiles in a Lossy Homogeneous Phantom Using a Dual-Mode Antenna With Integral Water Bolus

Svein Jacobsen and Paul R. Stauffer, *Member, IEEE*

***Abstract*—In the treatment of cancer, microwave hyperthermia has been established as an efficient adjunctive procedure to radiation therapy and chemotherapy. Wider acceptance of this method awaits schemes to measure volumetric temperatures noninvasively in human tissue for control of the heating process. This effort describes the design and performance of a new microstrip applicator intended for homogeneous heating of superficial tissue while at the same time monitoring temperature of the underlying tissue by noninvasive radiometric sensing of black-body radiation from the heated volume. Radiometric capabilities are assessed in terms of accuracy of up to six measured brightness temperatures applied in an inversion algorithm from which one-dimensional depth temperature profiles are generated. Based on radiometric signals recorded over the 1–4-GHz range, the temperature accuracy determined from statistical analysis of 200 realizations of the process is better than ± 0.2 °C to a depth of 5 cm in phantom. Aperture heating uniformity is assessed with electric field scans in a homogeneous muscle phantom. As long as sufficiently thin (<5 mm) water boli are used, SAR distributions at 1-cm depth in phantom extends effectively just outside the aperture perimeter, making this microstrip antenna an excellent building block element of larger multi-antenna array applicators.**

***Index Terms*—Archimedean spiral, hyperthermia, microwave applicator, noninvasive temperature monitoring, PCB antenna, radiometry, superficial heating.**

I. Introduction

LOCAL hyperthermia has been shown clinically effective in the treatment of cancer when delivered as an adjuvant to radiation and/or chemotherapy [1]–[3]. Since treatment efficacy is highly dependent on the minimum delivered dose whereas pain and other complications are connected to high dose levels [4]–[6], the uniformity of applicator heating is crucial for satisfying this narrow therapeutic window. Clinical trials of adjunctive hyperthermia have in the past demonstrated statistically significant improvement in complete response rates for relatively small tumors [2], [7], but have failed to make a major impact on the disease due to limitations in the size and location of tumors that can be heated effectively with current equipment. Similar difficulties in heating large or highly contoured areas of the body uniformly have restricted the use of moderate temperature hyperthermia for other clinical applications such as the treatment of psoriasis, which has also been shown responsive to heat therapy [8]–[10]. Consequently, the design and development of a lightweight and flexible printed circuit board (PCB) microstrip array applicator has been undertaken to treat large area superficial disease located over contoured surfaces of the human body. The heating capabilities of small subsections of such an array applicator have been reported previously in the form of finite-difference time-domain (FDTD) simulations and experimental measurements of power deposition patterns (SAR) in homogeneous muscle [11]–[13] as well as more realistic heterogeneous tissue loads [14]. The SAR patterns have been mapped into expected temperature distributions for a range of appropriate blood perfusion conditions using finite difference numerical solutions of the bioheat equation in [15]. While the dual concentric conductor (DCC) based conformal array applicator was originally designed for use at 915 MHz, the feasibility of using the same antenna array at an operating frequency of 433 MHz has also been investigated [16]. Although these publications allude to the possibility of heating large areas with up to 32 individually controlled microwave power sources, effective and quantitative clinical use has been hampered by the requirement for tedious thermal mapping of discreet fiberoptic probes across the antenna/skin–surface interface, in order to monitor temperatures and control power of the numerous array elements. In addition, the number and positions of thermometer probes that can be inserted *into* the patient's body (to assess temperature at depth) are limited by trauma considerations. Insertion and localization of thermometer probes are laborious and time-consuming tasks which even under optimum conditions still result in inadequate spatial sampling.

For all these reasons, the concept of a dual-mode applicator was introduced with both heating and noninvasive thermometry capabilities combined into one structure [17]–[20]. The noninvasive temperature sensing principle incorporated in this applicator is based on a passive scan of microwave black-body radiation (radiometry) from the subcutaneous tissue volume. An important limitation of this specific measurement technique is the *extremely* weak signal level that emanates from within lossy media ($\sim 10^{-12}$ W at $T = 40$ °C for a 500-MHz integration bandwidth). In our previously reported dual-mode antenna approach for radiometric thermometry, the sensing and heating an-

Manuscript received April 2, 2001.

S. Jacobsen is with the University of Tromsø, N-9037 Tromsø, Norway (e-mail: Svein.Jacobsen@phys.uit.no).

P. R. Stauffer is with the University of California, San Francisco, CA 94143 USA (e-mail: Stauffer@radonc17.ucsf.edu).

Publisher Item Identifier 10.1109/TMTT.2002.800424.

tennas were both located in the same plane on the back side of the bolus bag [18], [20], [21]. Hence, the radiometric signal faces energy mismatches at the two bolus walls and attenuation through the water bolus. Overlapping, multi-layer microstrip spiral antenna configurations have been investigated by Ryan [22] and Jacobsen and Stauffer [23]. The latter study, which looked at highly overlapped spirals, showed perturbation of the radiation patterns in the form of increased sidelobes. Here we describe a nonoverlapping, multilayer, stacked antenna design with the radiometer receive antenna located on the front (skin) surface of a thin water bolus and the heating antenna on the bolus back surface. Hence, this dual-purpose applicator incorporates the water bolus directly within the multilayer antenna structure. The investigation compares the heating and radiometric performance of this new integral bolus antenna with previous designs [18]–[21]. In this initial feasibility study, we report i) experimental measurements of power deposition patterns in a saline phantom and ii) estimated one-dimensional (1-D) depth temperature profiles in a solid TX-150 phantom as derived from brightness temperatures sampled in up to six 500-MHz bands in the range from 1 to 4 GHz.

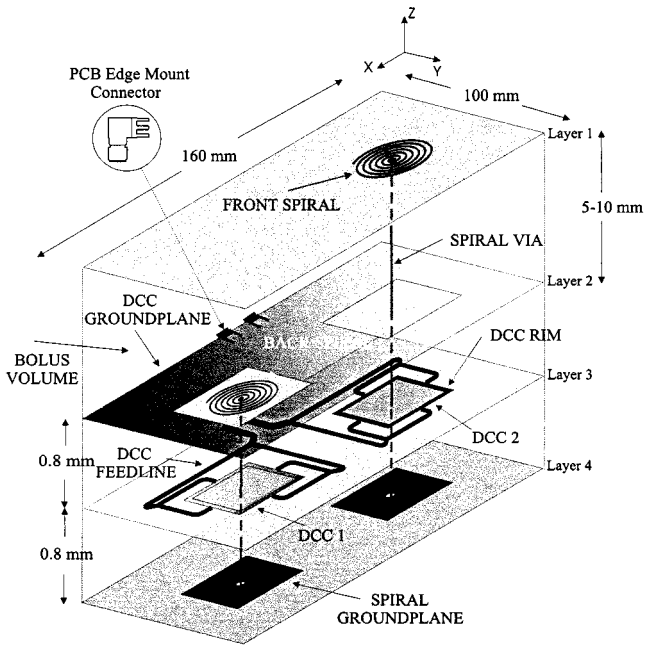

Fig. 1. Experimental dual-mode antenna test configuration to compare radiometric performance of front and back bolus surface mounted Archimedean spiral antennas.

II. Materials, Methods and Theory

A. Dual-Purpose Applicator Design

The device under test (DUT) in the current effort is one of two different configurations of a dual-mode PCB antenna with integral water bolus. In previous investigations, Dual-mode antennas were realized by etching a one-armed Archimedean spiral microstrip antenna from the central square part of a DCC aperture [18]–[20] and operated with an intervening water bolus between the antennas and test load. For the present study, a variant of the design was constructed by placing the radiometric probe (spiral) on the front side of the bolus immediately adjacent to the load while retaining the heating device (DCC) at the bolus back wall. In this configuration, the bolus liquid serves as a high permittivity substrate in addition to the two PCB dielectric layers between the spiral windings and ground plane. These two principally different antenna designs are diagramed in the test setup of Fig. 1. The dual-mode antenna configurations are paired as DCC 1 and back spiral (old design), and DCC 2 and front spiral (new design), respectively.

In order to accommodate the front surface spiral, the new dual-mode antenna design of Fig. 1 reveals important changes in the planar DCC antenna structure as well. In all previous work with DCC antennas, the inner and outer conductors were contained in the same plane. However, in Fig. 1, the 2.5-mm inner conducting rim is formed in the microstrip feedline layer (layer 3) rather than in the same plane as the outer conductor ground layer (layer 2). While not drawn to scale in the illustration, the three lower conducting layers are separated by 0.8-mm dielectric substrates whereas the two upper conducting layers are formed on opposite walls of the 5–10-mm-thick water bolus. The structures are connected electrically to microwave equipment by right angle SMA connectors placed conveniently along one edge of the PCB with ground connections to layer 2 and the center pins connected to the microstrip feedlines of layer 3. RF connections to the spirals are obtained using straight jack SMA connectors soldered to the back layer ground patches (layer 4) with small wires extending from the center pins through vias in the substrate to connect the centers of each Archimedean spiral.

A square slot outer dimension of 35×35 mm^2 is selected to produce a large and balanced effective field size (EFS) for the DCC at 915 MHz. For studies at 433 and 2450 MHz, the appropriate DCC dimensions are approximately 60×60 mm^2 and 20×20 mm^2, respectively.

The radiometric sensing elements incorporated into the hybrid structure are described by the Archimedean spiral function $r = \Gamma\phi_s$ (Γ: spiral constant, ϕ_s: winding angle). In addition to Γ, the strip width, substrate permittivity, antenna diameter, and substrate thickness are degrees of freedom in the design. From the rules of thumb on single-arm spiral antenna design outlined in [23], the following parameter values were selected: Spiral constant $\Gamma = 0.032$ cm, strip width $w = 0.6$ mm, substrate thickness $d = 0.8$ mm, permittivity $\epsilon_{rs} = 2.53$ (back spiral) and $\epsilon_{rs} = 77$ (front spiral), and antenna diameter $D = 28$ mm. Even though no attempts were made to optimize the designs with respect to antenna efficiency, the matching properties (return losses) were measured to be better than -10 dB (data not shown) in the operating bandwidth from 1 to 4 GHz.

B. Power Deposition Pattern Measurements

Radiated field distributions of the transmit-and-receive antennas were measured in a dissipative medium consisting of a 6-g/L saline solution. A computer controlled stepper motor based 3 axis scanning system was used to scan a passive monopole probe through the phantom in order to map E-field distributions as a function of space (0.5-mm precision) and frequency (205-MHz increments) in the frequency range from 900 to 5000 MHz. The probe was simply constructed [24] from a rigid coaxial cable (RG-141/U). The coax inner conductor,

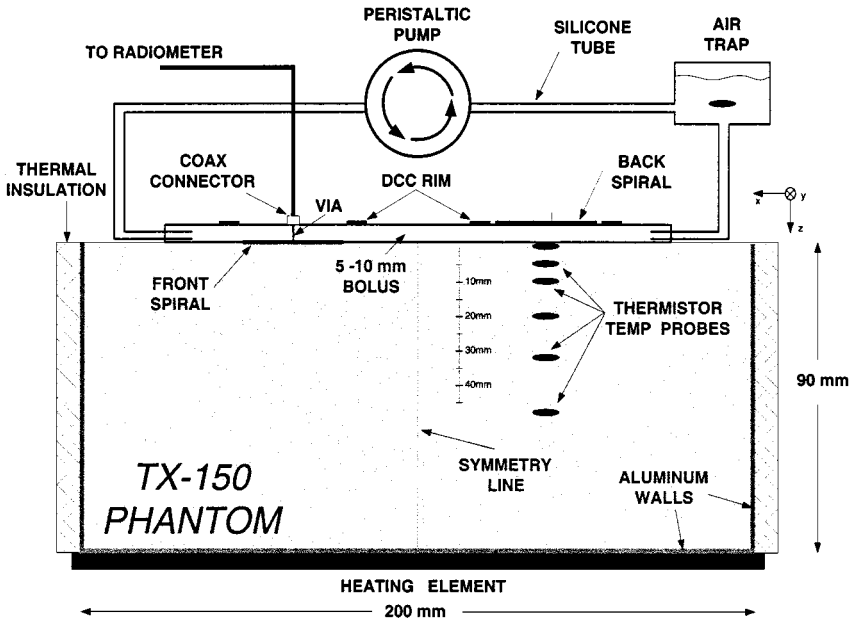

Fig. 2. Experimental setup used in temperature profile measurements. Phantom: TX-150.

covered by a polyethylene dielectric, extends approximately 10 mm (0.7 λ to 3.8 λ in phantom for the frequency ROI) beyond the end of the outer conductor to form a monopole sensor. Furthermore, the coupled signal from the probe was fed to a homodyne (phase and amplitude) detection system. The sensor configuration provided a spatial resolution of 2 mm perpendicular and 10 mm along the axis of the monopole, respectively. By rotating the probe 90° to three orthogonal positions, a mapping of the E_r-(radial), E_θ-(angular), and E_z-field (in depth) components was obtained in three sequential procedures. For each scan, the initial starting point for the center of the monopole was repeatable within $\pm$0.5 mm and $\pm$0.5°. The cross-polarization damping of the probe was determined to be $>$23 dB. Power deposition distributions were measured in the plane parallel to the applicator surface at $z = 1$-cm depth in phantom.

C. Radiometric Temperature Measurements and Instrumentation

Fig. 2 depicts the temperature measurement configuration considered in the present study. A solid TX-150 muscle equivalent phantom load with: 20 cm $\times$ 20 cm cross section and 9-cm height was placed on top of a heating element with controllable temperature. The four sidewalls, of highly conducting material (aluminum), were thermally insulated to minimize convection and radiation heat loss. Furthermore, the phantom structure was topped with the 10×16 cm^2 antenna array shown in Fig. 1. This arrangement allowed measurements of load temperature with the radiometric probe antenna either placed directly onto the load (front spiral), or coupled to the load through a 5–10-mm water bolus (back spiral). The lateral (transverse) temperature gradient was measured to be small compared to variations of temperature with depth in the phantom. Hence, the temperature distribution below the antenna could be considered plane-parallel at least within the radiometrically contributing phantom volume. For correlation with radiometric measurements, "true" 1-D depth profiles were established by means of 6 thermistor probes located in the upper 5 cm of the phantom. One additional thermistor probe was placed in the circulating bolus liquid (deionized water) to monitor temperature of this closed system. Radiometric measurements of the load brightness temperature were obtained for six independent frequency bands—each with an integration bandwidth of 500 MHz. The center frequencies were 1.25, 1.75, 2.25, 2.75, 3.25, 3.75 GHz. In each band, the radiometer output was sampled at a rate of 5 Hz over a 40-s time interval, giving 200 samples for further data processing and statistical evaluation. The accuracy of derived temperature profiles was compared for three different cases using: 1) all six frequency bands; 2) three frequency bands centered at 1.25, 1.75, and 2.25 GHz; and 3) two frequency bands centered at 1.25 and 2.25 GHz.

In order to prevent standing wave effects between the emitted phantom black body radiation and the thermistor probes, data were recorded initially for the front spiral in the setup of Fig. 2. The antenna structure was then rotated 180° in the horizontal (x–y) plane. Radiometric data for the back spiral were then generated, assuming that the insulated wall phantom exhibits symmetric temperature distributions about the line of symmetry.

The Dicke null-balancing radiometer prototype used in the experiments has been described in the literature previously [18]. However, to improve the overall system performance (brightness temperature resolution) substantially, the two original cascaded front end low-noise amplifiers (LNAs) were replaced by new devices[1] specified to have a noise figure as low as 0.89–1.1 dB over the 1–4-GHz band. With a detector integration time of 2 s and integration bandwidth of 500 MHz, the brightness temperature resolution $\sigma_{T_B}^{(i)}$ was measured to vary from 0.050 °C–0.056 °C.

[1]Miteq Corporation, Hauppauge, NY 11788, USA.

D. Radiometric Theory and Adaptation Scheme

Microwave radiometry used for noninvasive thermometry of living tissue is often given the notation "microwave thermography." The sensing technique is short-range and based on the detection of electromagnetic thermal noise emitted by sub-surface biological tissue. A microwave sensor connected to a radiometric receiver measures an effective (brightness) temperature determined from the weighted volumetric average of temperature within the sense volume. This average is spatially weighted due to a frequency dependent attenuation of the radiation intensity from every given observation point inside the body and the microwave sensor at the surface. Defining $T(\underline{r})$ as being the physical temperature of the object at point $\underline{r}$, the apparent temperature observed from outside is denoted brightness temperature $T_{B_{\mathrm{mod}}}$ and given by the radiometric equation [19]

$$T_{B_{\mathrm{mod}}}^{(i)} = \gamma^{(i)} \int_V W^{(i)}(\underline{r},\, f) T(\underline{r})\, dV + \gamma^{(i)} T_{EXT} + T_{INT} \tag{1}$$

where W is a weighting function defined over a volume V, f is the frequency, dV is an infinitesimal medium volume at position $\underline{r}$, γ is the antenna efficiency, T_{EXT} is the external picked up interference, and T_{INT} is the noise produced internally in the radiometer electronics. The superscript "i" indicates that radiometric observations can be made over different frequency bands Δf^i whereas the subscript "mod" signifies that this is a signal model. Furthermore, W is a nonnegative function normalized according to [26]

$$\int_V W^{(i)}(\underline{r},\, f)\, dV \equiv 1. \tag{2}$$

Note that the quotient between the first term in (1) and the latter two terms describing observed noise effects, is related to the signal-to-noise ratio of the observation points.

Utilizing (2) in (1), $\gamma^{(i)}$ were determined by heating the phantom volume in two steps to constant, homogeneous temperatures $T(\underline{r}) = 10$ and 20 °C above an initial temperature and recording ΔT_B^i at 6 selected frequency bands. In this case, T_B and the assumed known $T(\underline{r})$ are linearly related through γ. Furthermore, for the phantom in Fig. 2 we adopt a 1-D weighting function model of type

$$W^{(i)}(z) = \frac{1}{d^{(i)}} \exp\left(-\frac{z}{d^{(i)}}\right) \tag{3}$$

where $d^{(i)}$ is the upper theoretical power penetration depth given by $d^{(i)} = (1/\sigma^{(i)})\sqrt{\epsilon^{(i)}/\mu_0}$ with $\sigma^{(i)}$ and $\epsilon^{(i)}$ being the frequency dependent conductivity and permittivity of the sensing volume, respectively; and μ_0 the free-space permeability. Obviously, since a 3-D problem is represented by a 1-D model, $d^{(i)}$ must be regarded as the "effective sensing depth" taking both medium loss and antenna diffraction effects into account. $d^{(i)}$ were determined experimentally using a method outlined in [25].

E. Signal Processing

We wish to solve (1) with the constraints that

$$T_{B_{\mathrm{mod}}}^{(i)} \approx \hat{T}_B^{(i)}, \qquad \text{for } i = 1, 2, \ldots, N_b \tag{4}$$

where $\{\hat{T}_B^{(i)}\}$ is a set of single measured samples of the radiometer output. Here, N_b refers to the number of selected measurement bands. In practice $M \le N_b \le N_{\max}$ where M is the number of independent parameters in the temperature profile model and $N_{\max}$ the maximum number of nonoverlapping frequency bands. By the use of *a priori* knowledge on the temperature distribution in depth, it is possible to improve the precision of temperature estimation in (4), however, at the expense of generality of the numerical solution. For the heated phantom model in Fig. 2, an adequate and relatively simple model function adopted in the reported work may be expressed

$$T(z) = T_0 + \Delta T \cdot \log(1 + \alpha z), \qquad 0 \le z \le z_{\max} \tag{5}$$

where T_0 is the temperature at the water bolus-phantom interface and $[\Delta T, \alpha]$ govern the curvature and steepness of the temperature profile.

Now, define the error function (mean square deviation)

$$\varepsilon(T_0,\, \Delta T, \alpha) = \sum_{i=1}^{N_b} \left(T_{B_{\mathrm{mod}}}^{(i)} - \hat{T}_B^{(i)}\right)^2. \tag{6}$$

Without loss of generality, we assume that T_0 is known (can be found by direct contact thermocouple, thermistor, or fiber-optic probes) leaving ΔT and α to be determined.

Let $\mathbf{G}$ be defined as the gradient of the error function ε, $\mathbf{G} = \nabla\varepsilon$, and $\mathbf{\Psi} = (\Delta T,\, \alpha)$. By using a series expansion of the gradient $\mathbf{G}$ and requiring that it equals zero, we get

$$\nabla\varepsilon(\mathbf{\Psi}^*) = \mathbf{G}(\mathbf{\Psi}^*) \approx \mathbf{G}(\mathbf{\Psi}) + \nabla\mathbf{G}(\mathbf{\Psi})(\mathbf{\Psi}^* - \mathbf{\Psi}) = 0 \tag{7}$$

from which the optimum model parameters can be found by solving

$$\mathbf{\Psi}^* = \mathbf{\Psi} - \mathcal{H}^{-1}\nabla\varepsilon \tag{8}$$

where $\mathcal{H}_{i,\,j} = \partial^2\varepsilon/\partial\psi_i\partial\psi_j$ is the Hessian matrix. Equation (8) leads to the iterative adaptation algorithm

$$\mathbf{\Psi}_{m+1} = \mathbf{\Psi}_m - \mu\mathcal{H}_m^{-1}\nabla\varepsilon_m \tag{9}$$

with μ introduced as a convergence parameter to control stability and m is the iteration step.

Recalling the definitions of the error function and Hessian matrix, an adaptive procedure was derived for statistical evaluation of the 200 realizations of $\mathbf{\Psi}$ for *both* spiral antennas using different phantom model temperature profiles and $N_b = 2, 3,$ and 6 radiometric bands.

III. Results

Fig. 3 shows the measured 2-D power deposition patterns (SAR) 1-cm deep in phantom for the DCC 1 antenna directly coupled to the phantom surface (no bolus). The DCC antenna is dimensioned to produce a large EFS (area greater than or equal to 50% $\mathrm{SAR}_{\max}$) at 915 MHz. We note a broad central plateau between 50% and 75% of maximum SAR and a peripherally enhanced four corner peak heating pattern. At 2450 MHz, the SAR pattern is more peaky and exhibits a significantly smaller EFS, unsuitable for uniform heating since the aperture is physically too large compared

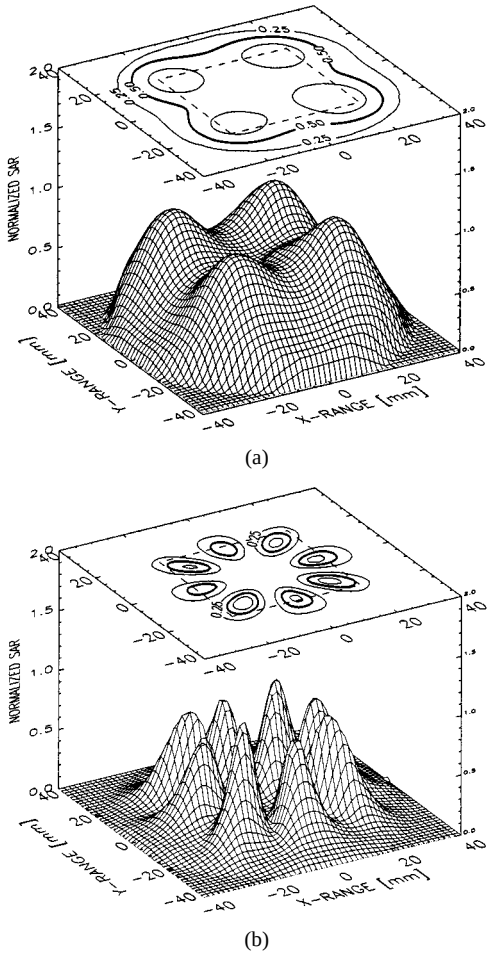

(a) (b)

Fig. 3. Power deposition patterns in 1-cm deep plane for DCC 1 aperture using no coupling bolus at both 915 MHz (upper panel) and 2450 MHz (lower panel).

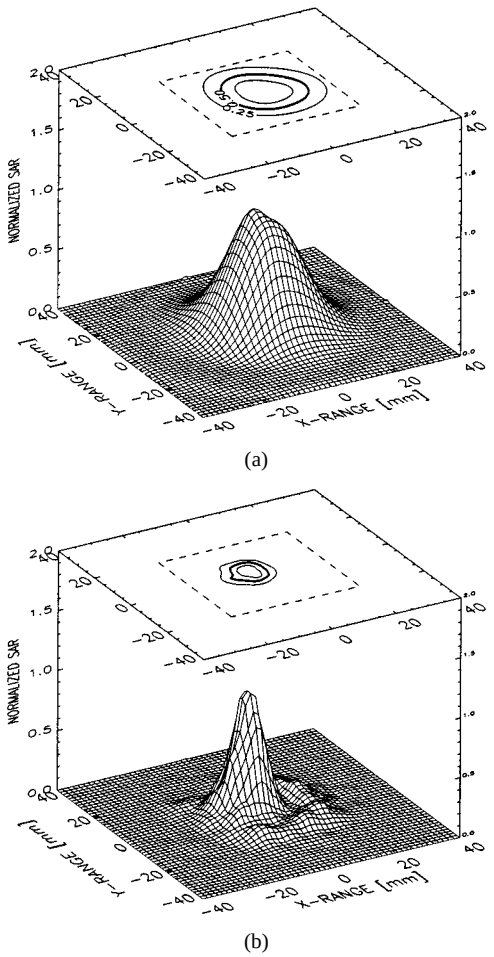

(a) (b)

Fig. 4. Power deposition patterns in 1-cm deep plane for back Archimedean spiral using no coupling bolus at both 915 MHz (upper panel) and 3770 MHz (lower panel).

to the corresponding lossy medium wavelength. In contrast, the direct coupled broad-band Archimedean spiral produces a centrally peaked radiation pattern that narrows (but retains its central peak) at higher frequencies as seen in Fig. 4. Fig. 5 (upper left panel) shows a representative SAR pattern for the back spiral radiating into phantom through a 5-mm water bolus below its critical frequency which was determined to be 1700 MHz. We observe a progressively worse damping and attenuation of the central peak at frequencies above 1700 MHz, splitting into a broader multi-peaked distribution (upper right panel). The front spiral exhibits a corresponding critical frequency of 2450 MHz, with similar perturbation of the central Gaussian patterns above that frequency (lower right panel).

Fig. 6 depicts the SAR patterns for both DCC antenna configurations at 915 MHz when radiating through 5-mm (upper panel) and 10-mm (lower panel) water bolus layers. Of particular note is that the peripherally enhanced four corner peak pattern of the direct coupled DCC apertures (Fig. 3, upper panel) is increasingly distorted and skewed toward the center of the antenna array as bolus thickness increases. Fig. 7 shows a typical example of brightness temperatures obtained from radiometric measurements of two different phantom temperature profiles, at 6 nonoverlapping frequency bands, using the front spiral antenna configuration.

After adaptive signal processing of data using (1) and (4), the corresponding estimated depth temperature profiles are shown in Fig. 8. We note that the mean temperature profiles (dashed lines) are biased slightly downwards from the true phantom temperatures (solid lines), though the error increases to a maximum of only -0.1 °C at 5-cm depth for both 1.5 °C and 3 °C gradients. In addition, the 68% confidence intervals are quite tight, spreading to only ± 0.2 °C at a depth of 5 cm for this front mounted spiral in direct contact with the phantom load.

To compare overall performance of the back and front spiral antennas as radiometric probes, the temperature accuracy $\sigma_{\hat{T}}$ and bias $B = T - \langle \hat{T} \rangle$, where "$\langle\ \rangle$" is the mean operator, were established using two, three, and six frequency band characterizations. Fig. 9 summarizes these performance indices. The front spiral performs quite acceptably with an accuracy of better than ± 0.32 °C for both profiles given that at least three bands are used. The bias absolute value is less than 0.1 °C for the three- and six-band measurements. As a direct consequence of a smaller signal-to-noise ratio, the back spiral exhibits somewhat less accuracy of ± 0.4 to ± 0.6 °C for the six- and two-band determinations, respectively. The bias is relatively small for six bands (~ -0.1 °C), but increases to -0.2 to -0.3 °C for fewer bands.

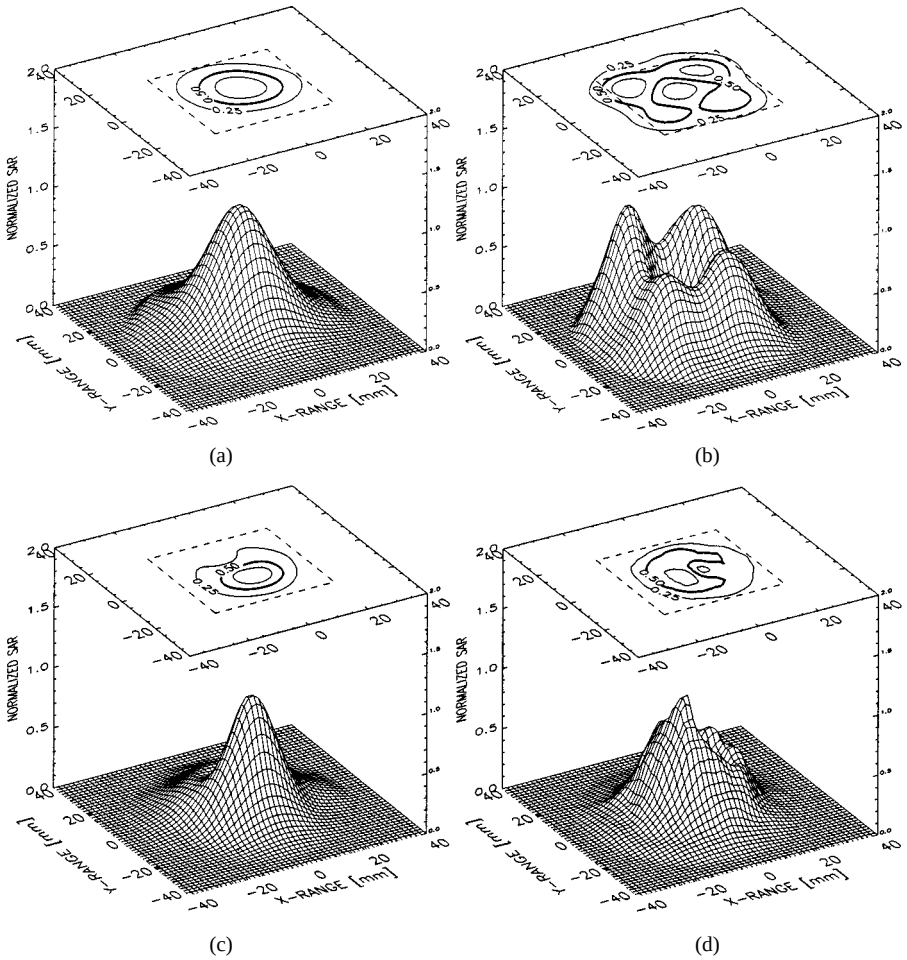

Fig. 5. Same as Fig. 4 for spiral antennas illuminating the phantom through a 5-mm deionized water bolus. Upper panels: back spiral, lower panels: front spiral. (a) 1310 MHz. (b) 2540 MHz. (c) 1925 MHz. (d) 3155 MHz

IV. Discussion

Single and multiple frequency radiometry have been proposed for accurate, noninvasive retrieval of predictably shaped temperature distributions [27], [28]. Another possible scheme is to use different sized antennas and utilize the fact that diffraction effects (and, hence, weighting functions) vary with the lateral dimension of the antenna [29], [30].

Radiometry can in principle be applied to derive fine-structure temperature variations in space and time, provided that a sufficient amount of data (different antenna positions and sampling frequencies) are available. However, radiometric data are usually sparse (2–6 samples) and highly contaminated with noise. Hence, the inverse problem, $T_B^{(i)} \rightarrow T(z)$, is ill-conditioned (prone to exhibit large variability) and use of *a priori* knowledge has been suggested as a basis for parametric modeling of temperature profiles with a reduced number of unknown variables [31], [32].

The adaptation problem formulated in (6) was solved by a method of steepest descent. Closer investigation of the error-performance surface shows several local minima of this function that yield approximately the same performance (data fit). Curve fitting problems in a multi-dimensional space can also be solved by a method called *regularization of ill-posed problems*, where the basic idea is to stabilize the solution by a selected non-negative functional that embeds prior information. This scheme, which often is denoted a Tikhonov approach [33], comprises two terms in which the first is the standard error term as in (6), and the second is a regularizing term that induces smoothness into the adaptive algorithm. Since both the input and output domains in the mapping from $T(z) \rightarrow T_B^{(i)}$ already are limited in range by the smooth parametric temperature profile in (5), we have chosen *not* to incorporate further regularization of the problem by a Tikhonov approach. However, as the inversion problem increases in complexity (temperature mapping in a 3-D heterogeneous medium) this generalization might be imperative.

The desired temperature accuracy (resolution) of invasive thermometry for superficial hyperthermia has been defined previously as ± 0.2 °C [34], [35]. For noninvasive thermometry, on the other hand, consensus has not yet been obtained on the required accuracy, due to the evolving technology and limited clinical use today of such thermometry. It is quite reasonable to expect that the desired accuracy of noninvasive temperature measurement will be less stringent (perhaps on the order of 0.5 °C–1.0 °C) since the reading represents a volumetric average value of spatially varying temperatures. The accuracy of tissue temperatures measured noninvasively in lossy media by the radiometric technique is inversely proportional to the sensing depth. At the same time, the sensing principle is

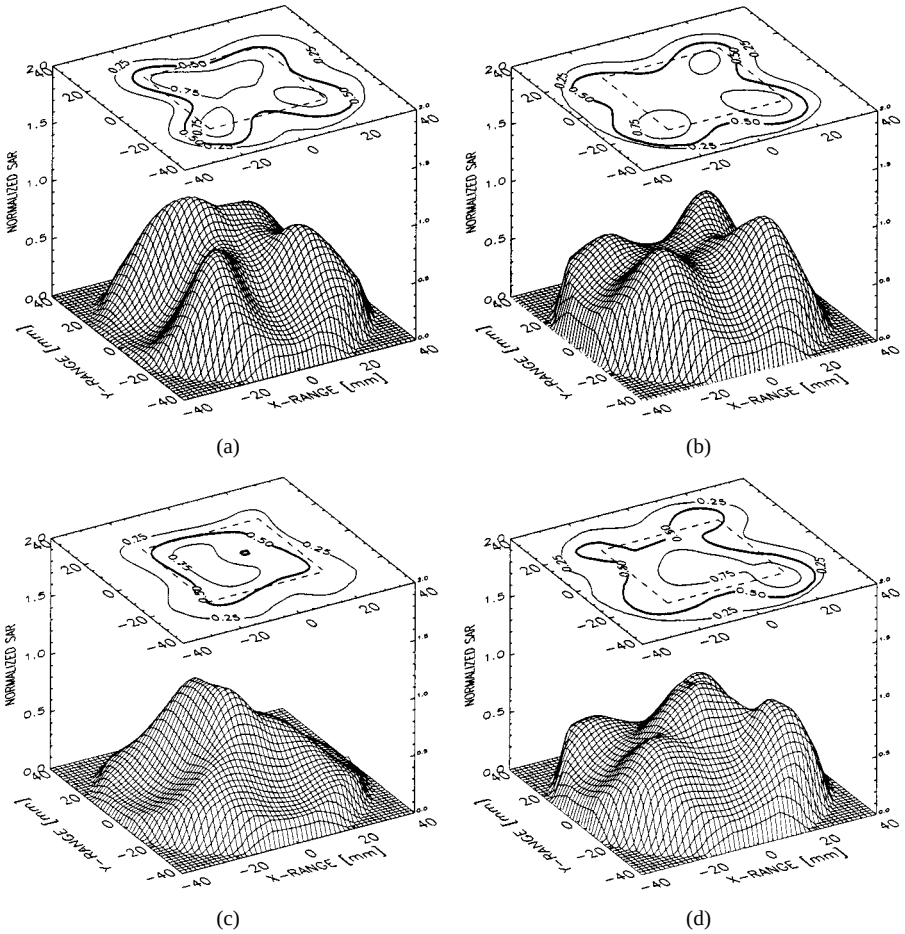

Fig. 6. Same as Fig. 3 for both DCC antennas scanned at 915 MHz using 5-mm and 10-mm deionized water boli. Right panels: DCC 1, left panels: DCC 2, upper panels: 5-mm bolus, lower panels: 10-mm bolus.

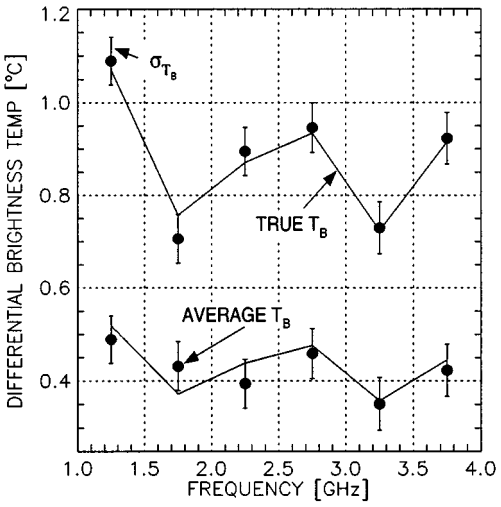

Fig. 7. Measured increase in brightness temperature above initial steady state values. σ_{T_B}: standard deviation, (•): T_B average value, (—): true brightness temperature.

influenced by a number of factors including: 1) brightness temperature minimum resolution; 2) external electromagnetic interference from other sources; 3) antenna size (lateral spatial resolution versus sensing depth); 4) antenna efficiency; 5) antenna bandwidth and medium matching properties; 6) cable loss (diameter and length); 7) radiometer integration bandwidth; 8) recording time (output filter bandwidth); 9) number of independent measurements (radiometer frequency bands); and 10) bolus versus radiometric signal interference (thickness, signal loss, reflections, back and front layer impedance mismatch). In this paper, the latter two items are focused on. If we compare the power deposition patterns of the investigated antennas with the more symmetric "control" scans obtained when the bolus is removed, a number of eye-catching features are apparent. Firstly, we observe a splitting of the central peak above the critical frequency of 1700 MHz for the back spiral radiating through the 5-mm water bolus. Gelvich and Mazokhin [36] discuss oscillation modes and resonance effects induced in the water bolus layers and how they influence SAR patterns. One of their main findings is that there exists a minimum critical bolus thickness (d_c) above which resonance effects can be induced. To first order, d_c is dependent primarily on the medium properties and signal frequency. However, to higher orders also additional resonance modes may be excited. These are a direct function of the bolus dimensions.

Typical effects on the power deposition patterns are damping of the SAR centrally and increasing asymmetry when the bolus thickness exceeds d_c. This feature is seen in Fig. 6 for the DCC configurations. With a distance of only 2.2 cm from the antenna periphery to the bolus edge, it is likely that energy can be constructively or destructively focused in this peripheral region as discussed by [36]. Additional distortion and SAR asymmetry

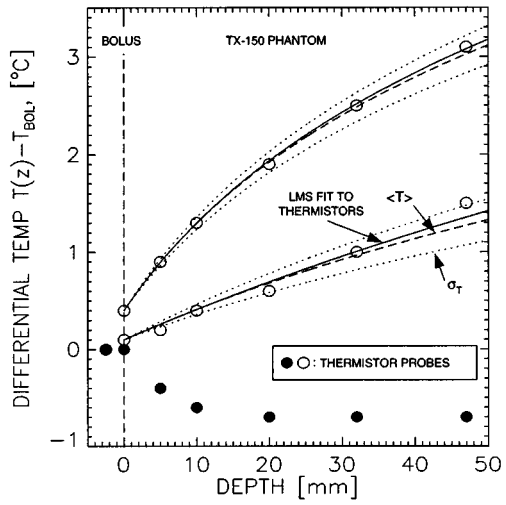

Fig. 8. Estimated depth temperature profiles based on data in Fig. 7. (•: initial) and (∘): thermistor based temperature measurements. (- - -): average of T, (· · · · · ·): one standard deviation, (—): LMS fit to thermistor values.

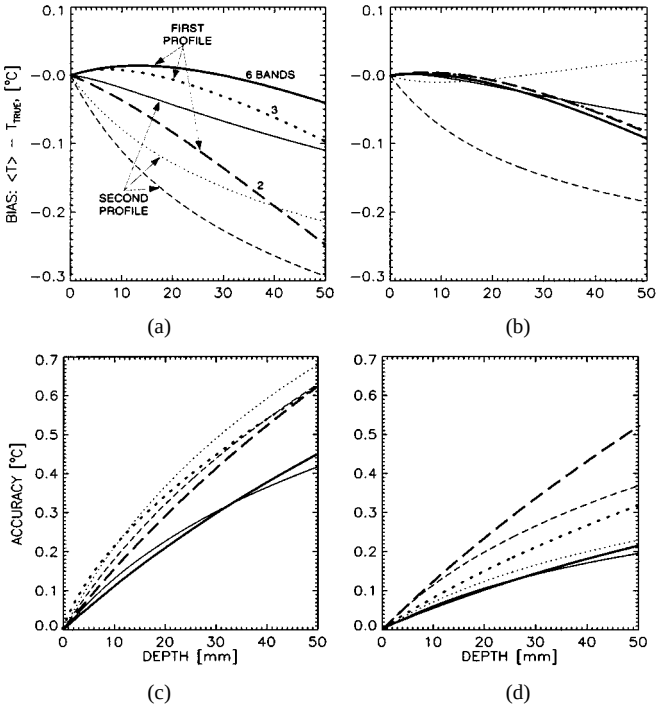

Fig. 9. Statistical bias and accuracy of radiometric temperature estimator in two temperature profiles using direct and 5-mm bolus coupled spiral sense antennas. Thick lines: first profile, thin lines: second profile, (—): six bands, (· · · · · ·): three bands, (- - -): two bands. (a), (c) Back spiral. (b), (d) Front spiral.

may result from interference between the radiating DCC aperture and spiral copper trace. These latter two effects are fortunately minor for the 5-mm bolus and do not hamper use of this proposed antenna structure for heating and radiometry purposes. However, for the 10-mm bolus, the situation is worse, with enhanced SAR centrally and further skewed radiation patterns. The configuration with a front surface mounted spiral placed flush against the medium is significantly different. In this case (see Fig. 5), the damped central region of SAR can *not* be explained by volume or standing wave oscillations in the water bolus since the spiral is in direct contact with the medium. It has already been documented however that printed circuit board microstrip antennas can convert a principal fraction of fed power into surface waves at a poorly matched antenna-medium interface. Coupling of power to surface waves has been reported to contribute to losses in coplanar waveguide and stripline antennas [37]. The substrate thickness h and permittivity ϵ_r should be chosen such that $h\sqrt{\epsilon_r} < 0.12\lambda_0$, where λ_0 is the free-space wavelength, to prevent excitation of surface waves [38]. With $h = 5$ mm and $\epsilon_r \approx 77$, frequencies above 58 MHz will induce such effects. Hence, operating from 900 to 5000 MHz, it is likely that surface wave modes are responsible for the observed interference in power deposition patterns from the front spiral high-permittivity thick substrate design. Although SAR perturbations are present in a wide band (1700–5000 MHz), these effects do not seem to be detrimental to the radiometric performance of the antenna as observed in Figs. 8 and 9.

When discussing the performance of microwave radiometry applied as a noninvasive thermometry scheme, two pertinent quantities are the statistical spread and bias of the estimated, compared to actual, temperature profiles. Fig. 9 summarizes these features for the two different antenna configurations that were investigated in this work. Overall, the spiral placed flush to the heated medium performs significantly better than the back spiral sensing through the water bolus. This is to be expected *a priori* since the signal-to-noise ratio is a factor of two larger for the contact probe. As also may be anticipated from a statistical evaluation of the least-mean-square (LMS) fit problem, fewer measurement bands introduce larger variations and instabilities in the adaptation algorithm. For the back spiral, two frequency band case, well-considered initial parameter guesses were required to assure stability in the iterative inversion algorithm. For the front spiral, six frequency band case, the steepest-descent algorithm converges very fast in fewer iteration steps (10–20) to parameter values very close to the actual ones. While these tests showed marginally acceptable accuracy for two bands in a homogeneous phantom with essentially a 1-D temperature gradient, clinical measurements of 3-D temperature distributions in a heterogeneous medium will likely exhibit larger errors. This may require at least three or maybe as many as six band radiometry to obtain sufficient 1-D profile temperature accuracy to depths of 5 cm in lossy tissue.

V. Conclusions

In this paper, we introduce a dual-mode microwave transceiving antenna design for simultaneous heating and noninvasive thermometry of superficial tumors. The design is conceptually different from previous designs in that the temperature sensing antenna and heating antenna are placed on opposite sides of the water bolus, with the former in direct contact with the medium. This approach increases the radiometric signal sensitivity by approximately a factor of two. A comparison of the performance of this design to a more conventional realization, where both antenna elements are placed concentrically in one plane on the back surface of the coupling bolus, shows that the temperature accuracy can be improved from typically ± 0.4 °C to ± 0.2 °C at 5-cm depth in phantom when six independent frequency bands are

used in the temperature inversion algorithm. The second part of the investigation included determination of the transceiving antenna power deposition patterns. Data indicate that SAR patterns are only marginally perturbed by the presence of a narrow spiral copper trace placed in the central area of the DCC heating aperture, whether on the back or front surface of bolus. Spurious volume and surface standing wave oscillations in the water bolus layer appear to be of greater importance, producing significant perturbation of the SAR when thick ($\geq$10 mm) bolus layers are used. When the bolus thickness is reduced to 5 mm or less, the power deposition patterns of DCC antennas are essentially unperturbed relative to the direct coupled case.

With an improved accuracy of temperature detection and minimal perturbations of heating antenna SAR patterns, the front surface mounted spiral Dual-Mode antenna introduced in this work has the potential to represent a nearly ideal building block element of large-area array applicators for combined heating and multifrequency radiometry.

REFERENCES

[1] P. K. Sneed, P. R. Stauffer, G. C. Li, and G. J. J. Stege, *Hyperthermia, in Textbook of Radiation Oncology*, S. A. Liebel and T. L. Philips, Eds. Philadelphia, PA: Saunders, 1998, pp. 1241–1262.

[2] C. C. Vernon, J. W. Hand, S. B. Field, D. Machin, J. B. Whaley, J. van der Zee, W. L. J. van Putten, G. C. van Rhoon, J. D. P. van Dijk, D. Gonzalez-Gonzalez, F. F. Liu, P. Goodman, and M. Sherar, "Radiotherapy with or without hyperthermia in the treatment of superficial localized breast cancer. Results from five randomized controlled trials," *Int. J. Rad. Oncol. Biol. Phys.*, vol. 35, no. 4, pp. 731–744, 1996.

[3] J. van der Zee, D. Gonzalez-Gonzalez, G. C. van Rhoon, J. D. P. van Dijk, W. L. J. van Putten, and A. A. M. Hart, "Comparison of radiotherapy alone with radiotherapy plus hyperthermia in locally advanced tumors: A prospective, randomized, multicentre trial," *Lancet*, vol. 355, pp. 1119–1125, 2000.

[4] K. A. Leopold, M. W. Dewhirst, T. V. Samulski, R. K. Dodge, S. L. George, J. L. Blivin, L. R. Prosnitz, and J. R. Oleson, "Cumulative minutes with T90 greater than Tempindex is predictive of response of superficial malignancies to hyperthermia and radiation," *Int. J. Rad. Oncol. Biol. Phys.*, vol. 25, no. 5, pp. 841–847, 1993.

[5] J. R. Oleson, T. V. Samulski, K. A. Leopold, S. T. Clegg, M. W. Dewhirst, R. K. Dodge, and S. L. George, "Sensitivity of hyperthermia trial outcomes to temperature and time: Implications for thermal goals of treatment," *Int. J. Rad. Oncol. Biol. Phys.*, vol. 25, no. 2, pp. 289–297, 1993.

[6] M. W. Dewhirst and D. A. Sim, "The utility of thermal dose as a predictor of tumor and normal tissue responses to combined radiation and hyperthermia," *Cancer Res. (Suppl.)*, vol. 44, pp. 4772–4780, 1984.

[7] C. A. Perez, T. Pajak, B. Emami, N. B. Hornback, L. Tupchong, and P. Rubin, "Randomized phase III study comparing irradiation and hyperthermia with hyperthermia alone in superficial measurable tumors. Final report by the Radiation Therapy Oncology Group," *Amer. J. Clinical Oncol.*, vol. 14, no. 2, pp. 133–141, 1991.

[8] D. R. Boreham, H. C. Gasman, and R. E. J. Mitchel, "Water bath hyperthermia is a simple therapy for psoriasis and also stimulates skin tanning in response to sunlight," *Int. J. Hyperthermia*, vol. 11, no. 6, pp. 745–754, 1995.

[9] E. K. Orenberg, F. R. Noodleman, J. A. Koperski, D. Pounds, and E. M. Farber, "Comparison of heat delivery systems for hyperthermia treatment of psoriasis," *Int. J. Hyperthermia*, vol. 2, no. 3, pp. 231–241, 1986.

[10] A. Urabe, K. Nishitani, and K. Hohda, "Hyperthermia in the treatment of psoriasis," *Acta Dermatology*, vol. 117, pp. 770–774, 1981.

[11] F. Rossetto, P. R. Stauffer, V. Manfrini, C. J. Diederich, and G. B. Gentili, "Effect of practical layered dielectric loads on SAR patterns from dual concentric conductor microstrip antennas," *Int. J. Hyperthermia*, vol. 14, no. 6, pp. 553–571, 1998.

[12] P. R. Stauffer, M. Leoncini, V. Manfrini, G. B. Gentili, C. J. Diederich, and D. Bozzo, "Dual concentric conductor radiator for microwave hyperthermia with improved field uniformity to periphery of aperture," *IEICE Trans. Commun.*, vol. E78-B, no. 6, pp. 826–835, 1995.

[13] P. R. Stauffer, F. Rossetto, M. Leoncini, and G. Biffi Gentilli, "Radiation patterns of dual concentric conductor microstrip antennas for superficial hyperthermia," *IEEE Trans. Biomed. Eng.*, vol. 45, pp. 605–613, May 1998.

[14] F. Rossetto and P. R. Stauffer, "Effect of complex bolus-tissue load configurations on SAR distributions from dual concentric conductor applicators," *IEEE Trans. Biomed. Eng.*, vol. 46, pp. 1310–1319, Nov. 1999.

[15] F. Rossetto, C. J. Diederich, and P. R. Stauffer, "Thermal and SAR characterization of multielement dual concentric conductor microwave applicators for hyperthermia, a theoretical investigation," *Med. Phys.*, vol. 24, no. 2, pp. 745–753, 2000.

[16] F. Rossetto and P. R. Stauffer, "Theoretical characterization of dual concentric conductor microwave applicators for hyperthermia at 433 MHz," *Int. J. Hyperthermia*, vol. 17, no. 3, pp. 258–270, 2001.

[17] S. Jacobsen, A. Murberg, and P. R. Stauffer, "Characterization of a transceiving antenna concept for microwave heating and thermometry of superficial tumors," *Progress in Electromagn. Res.*, vol. PIER 18, pp. 105–125, 1998.

[18] S. Jacobsen, P. Stauffer, and D. Neuman, "Dual-mode antenna design for microwave heating and noninvasive thermometry of superficial tissue disease," *IEEE Trans. Biomed. Eng.*, vol. 47, pp. 1500–1509, Nov. 2000.

[19] ——, "Transceiving antenna for homogeneous heating and radiometric thermometry during hyperthermia," *Electron. Lett.*, vol. 36, no. 6, pp. 496–497, 2000.

[20] P. Stauffer, S. Jacobsen, F. Rossetto, C. Diederich, and D. Neuman, "Dual mode antenna array for microwave heating and noninvasive thermometry of superficial tissue disease," in *Proc. SPIE Thermal Treatment of Tissue With Image Guidance*, vol. 3594, T. P. Ryan and T. Z. Wong, Eds., 1999, pp. 139–147.

[21] P. R. Stauffer, S. Jacobsen, and D. Neuman, "Microwave array applicator for radiometry controlled superficial hyperthermia," in *Proc. SPIE Thermal Treatment of Tissue: Energy Delivery and Assessment*, vol. 4247, T. P. Ryan, Ed., 2001, pp. 19–29.

[22] T. P. Ryan, V. L. Backus, and C. T. Coughlin, "Large stationary microstrip arrays for superficial microwave hyperthermia at 433 MHz: SAR analysis and clinical data," *Int. J. Hyperthermia*, vol. 11, no. 2, pp. 187–209, 1995.

[23] S. Jacobsen and P. Stauffer, "Improved spatial resolution in thermography obtained by a two-layered structure of microstrip spirals," *J. Electromagn. Waves and Applications*, vol. 13, no. 3, pp. 307–323, 1999.

[24] J. R. James and P. S. Hall, *Handbook of Microstrip Antennas*: Peregrinius, 1989, vol. 2.

[25] S. Mizushina, T. Shimizu, K. Suzuki, M. Kinomura, H. Ohba, and T. Sugiura, "Retrieval of temperature-depth profiles in biological objects from multi-frequency microwave radiometric data," *J. Electromagn. Waves Applicat.*, vol. 7, no. 11, pp. 1515–1547, 1993.

[26] F. Bardati, V. J. Brown, and P. Tognolatti, "Temperature reconstruction in a dielectric cylinder by multi-frequency microwave radiometry," *J. Electromagn.Waves Applicat.*, vol. 7, no. 11, pp. 1549–1571, 1993.

[27] M. Plancot, B. Prevost, M. Chivé, J. J. Fabre, R. Ledee, and G. Giaux, "A new method for thermal dosimetry in microwave hyperthermia using microwave radiometry for temperature control," *Int. J. Hyperthermia*, vol. 3, no. 1, pp. 9–19, 1987.

[28] L. Dubois, J. Priebetich, J. J. Fabre, M. Chivé, and Y. Moschetto, "Noninvasive microwave multifrequency radiometry used in microwave hyperthermia for bidimensional reconstruction of temperature patterns," *Int. J. Hyperthermia*, vol. 9, no. 3, pp. 415–431, 1993.

[29] B. Bocquet, P. Dehour, A. Mamouni, J. C. van de Velde, and Y. Leroy, "Near-field microwave radiometric weighting functions in multilayered materials," *J. Electromagn. Waves Applicat.*, vol. 7, no. 11, pp. 1497–1514, 1993.

[30] A. Mamouni, F. Bliot, Y. Leroy, and Y. Moschetto, "A modified radiometer for temperature and microwave properties measurement of biological substances," in *Proc. 7th Eur. Microwave Conf.*, Copenhagen, Finland, 1977.

[31] H. Ohba, M. Kinomura, M. Ito, T. Sugiura, and S. Mizushina, "Multifrequency microwave radiometry for noninvasive thermometry using a new temperature profile model function," *IEICE Trans. Elec.*, vol. E78-C, no. 8, pp. 1071–1081, 1995.

[32] A. Materka and S. Mizushina, "Parametric signal restoration using artificial neural networks," *IEEE Trans. Biomed. Eng.*, vol. 43, pp. 357–372, Apr. 1996.

[33] A. Tikhonov, "On regularization of ill-posed problems," *Doklady Akad. Nauk USSR*, vol. 153, pp. 49–52, 1973.

[34] J. W. Hand, J. J. W. Lagendijk, J. B. Andersen, and J. C. Bolomey, "Quality assurance guidelines for ESHO protocols," *Int. J. Hyperthermia*, vol. 5, no. 4, pp. 421–428, 1989.

[35] P. Shrivastava, K. Luk, J. Oleson, M. Dewhirst, T. Pajak, B. Paliwal, C. Perez, S. Sapareto, T. Saylor, and R. Steeves, "Hyperthermia quality assurance guidelines," *Int. J. Rad. Oncol. Biol. Phys.*, vol. 16, no. 3, pp. 571–587, 1989.

[36] E. A. Gelvich and V. N. Mazokhin, "Resonance effects in applicator water boluses and their influence on SAR distribution patterns," *Int. J. Hyperthermia*, vol. 16, no. 2, pp. 113–128, 2000.

[37] P. Perlmutter, S. Shtrikman, and D. Treves, "Electric surface current model for the analysis of microstrip antennas with the application to rectangular elements," *IEEE Trans. Antennas Propagat.*, vol. AP-33, pp. 301–311, Mar. 1985.

[38] M. Riaziat, R. Majidiahy, and I. J. Feng, "Propagation modes and dispersion characteristics of coplanar waveguides," *IEEE Trans. Microwave Theory Tech.*, vol. MTT-38, pp. 245–251, Mar. 1990.

Svein Jacobsen was born in Lofoten, Norway, in 1958. He received the B.Sc. and M.Sc. degrees from the University of Tromsø, Norway, in 1983 and 1985, respectively, and the Ph.D. degree on microwave sensing of the ocean surface, also from the University of Tromsø, Norway, in 1988.

From 1989 to 1992, he was engaged as a Scientist for the Norwegian Research Council for Science and Humanities, working with nonlinear mapping of the ocean surface by means of synthetic aperture radar (SAR). In 2000–2001, he did a research sabbatical at the University of California, San Francisco, where he investigated the use of radiometry for temperature measurement. He is currently a Professor in the Group of Electrical Engineering of the Department of Physics, University of Tromsø. His current research lies in the development of microwave applicators for heating superficial tumors and temperature mapping of the human body using microwave radiometry.

Paul R. Stauffer (M'81) received the B.A. degree in physics from the College of Wooster, Wooster, OH, in 1975 and the M.S.E.E. degree in engineering from the University of Arizona, Tucson, in 1979. Additional specialization led to Board Certification in clinical engineering in 1983 and medical physics in 1991.

He is currently Associate Professor in the Department of Radiation Oncology and also the Director of Physics and Engineering for Hyperthermia at the University of California, San Francisco. His current research interests include the engineering development and testing of RF, microwave and ultrasound applicators for uniform heat treatment of superficial and deep lying tissues. He has published over 100 papers and book chapters in the field of hyperthermia, and is an Associate Editor for the *International Journal of Hyperthermia*.